

Electrical characterization of porous La-doped BaSnO₃ using impedance spectroscopy

Md. Jawed Ansaree¹ · Shail Upadhyay¹

Received: 20 February 2015 / Revised: 6 May 2015 / Accepted: 25 May 2015 / Published online: 18 June 2015
© Springer-Verlag Berlin Heidelberg 2015

Abstract A few compositions in the system Ba_{1-x}La_xSnO₃ ($x=0.00, 0.01, 0.05, \text{ and } 0.10$) have been synthesized via the solid state ceramic route. The synthesized powders have been characterized using X-ray diffraction, scanning electron microscopy, energy-dispersive X-ray analysis, Raman spectroscopy, Fourier transformation infrared, thermogravimetical analysis, and differential thermal analysis techniques. The powder X-ray diffraction pattern of the samples confirms the formation of a single-phase solid solution only up to $0.50 \leq x$. It was found that all the samples have a cubic crystal structure. The electrical properties of La-modified BaSnO₃ were studied using ac impedance spectroscopy technique over a wide range of temperatures (50–650 °C) in the frequency range of 10 Hz–13 MHz. The complex impedance plots above 300 °C show that total impedance is due to the contributions of grain and grain boundaries. The resistance of these contributions has been determined. Variation of these resistances with temperature shows the presence of two different regions with different slopes. The nature of the variation of conductivity of the grain and grain boundaries is different in different regions. Based on the value of activation energy, it is proposed that conduction via hopping of doubly ionized oxygen vacancies (V_O^{**}) is taking place in the temperature region of 300–450 °C, whereas in the temperature region of 450–650 °C, it is due to proton, i.e., OH⁺ ions, hopping.

Keywords Perovskite oxides · Barium stannate · FTIR · DTA · Raman spectroscopy · Impedance spectroscopy

Introduction

Barium stannate and its solid solutions (e.g., BaTi_{1-x}Sn_xO₃) have found important applications in materials science and technology due to their dielectric properties [1–5]. Pure and doped barium stannate can be used as material for semiconductor gas sensors. It has been reported that sensors based on BaSnO₃ are sensitive to a variety of gases, e.g., CO, O₂, C₂H₅OH, CH₃SH, LPG, and NO_x [6–12]. Additionally, the results by Borse et al. [13, 14] and Yuan et al. [15] suggest that BaSnO₃-based systems could be candidates for photocatalytic applications. Mizoguchi et al. [16] reported that BaSnO₃ exhibits strong near-infrared luminescence at room temperature. Recently, barium stannate-based systems BaSn_{1-x}M_xO_{3-δ} (where M=Fe, Sc, In, Y, Gd, Sm, Nd, and La) have been proposed as proton conductors with potential applications in the fuel cell [17–20].

From the literature survey, it has been noticed that lanthanum can be a substitute for both barium and tin sites in barium stannate. Lanthanum substituted on the tin site of the barium stannate, BaSn_{1-x}La_xO_{3-δ}, system has been proposed as a proton conductor with potential applications in the fuel cell [21–24]. In these studies, the electrical characterization of the materials is done using complex plane impedance spectroscopy. This technique is used to separate out the contribution of grains and grain boundary resistances and measure the activation energy for conduction within the bulk and grain boundaries separately.

Lanthanum substituted for barium in the perovskite-type Ba_{1-x}La_xSnO₃ solid solution has been thoroughly

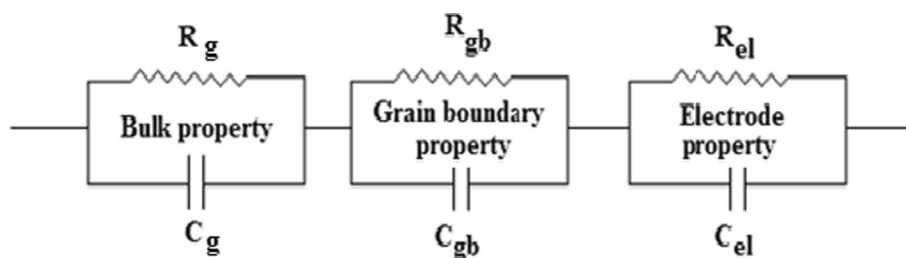
✉ Shail Upadhyay
supadhyay.app@itbhu.ac.in; shail72@yahoo.com

¹ Department of Physics, Indian Institute of Technology, Banaras Hindu University, Varanasi 221005, Uttar Pradesh, India

investigated [25–30]. Electrical and thermal properties of this system have been measured in a wide range of temperatures (4.2 K to 1100 °C). The literature survey indicates that the electrical properties of this system have basically been studied by conventional (dc) methods. A few reports are available on the characterization of this system by impedance spectroscopy but only up to 300 °C [31]. However, a systematic analysis of electrical properties by impedance analysis has not been carried out at high temperatures (above 300 °C). The present paper reports our investigations on electrical properties of lanthanum-doped barium stannate, $\text{Ba}_{1-x}\text{La}_x\text{SnO}_3$. The impedance analysis approach has been used to separate out the contribution of grains and grain boundary resistance to the total resistance. This technique is used to separate out the contribution of grains and grain boundary resistance and measure the activation energy for conduction within the bulk and grain boundaries separately.

The impedance spectrum and electrical conductivity have been observed as a function of temperature (50–650 °C) and frequency (10 Hz–13 MHz).

Complex plane impedance spectroscopy is considered to be a promising non-destructive testing method for analyzing the electrical processes occurring in a compound on the application of an a.c. signal as input perturbation. The output response of a polycrystalline compound represents grain, grain boundary, and interfacial properties with a different time constant. Using this technique, one can measure resistance due to grain interiors, grain boundaries, and the electrode independently. From these data and knowledge of the sample dimensions, the bulk (or grain interior) and grain boundary conductivities can be estimated in a rather straightforward manner. The equivalent electrical circuit shown below is widely used to fit impedance data of polycrystalline materials. In this equivalent circuit, it is desired to separate each of the RC components and measure values. *



Complex plane impedance plots (Z' vs. Z'') of many polycrystalline materials exhibit an arc at high frequencies, a second arc at lower frequencies, and a third arc at even lower frequencies. In a complex plane impedance plot, the ideal semicircle (whose center lies on the Z' axis) appears only when the contribution to this arc is having a single relaxation time. If the distribution of relaxation times exists, then one gets a depressed arc instead of the ideal semicircle. The frequency at the apex of each of the arcs corresponds to the characteristic frequency, ω_o of the respective (RC) subcircuit. The characteristic frequency, ω_o , of a material or a region of a material is equal to $1/RC$. Since R and C depend on geometric parameters in an inverse manner, therefore, ω_o is an intrinsic material property, independent of geometric consideration, and equal to $1/\rho\epsilon_o\epsilon_r$ (where ρ , resistivity, is equal to $1/\sigma$, ϵ_o is the permittivity of free space, and ϵ_r is the relative permittivity of material).

Experimental

Sample preparation

Samples with compositions $x=0.00, 0.01, 0.05,$ and 0.10 in the lanthanum-doped barium stannate system, $\text{Ba}_{1-x}\text{La}_x\text{SnO}_3$,

have been synthesized using the solid state ceramic method. The abbreviated names in the figures and text for samples with $x=0.00, 0.01, 0.05,$ and 0.10 are BS, BSL1, BSL5, and BSL10, respectively. The compounds used for the preparation of these samples are BaCO_3 (Merck, India, purity 99.0 %), SnO_2 (Sigma-Aldrich, USA, purity 99.9 %), and La_2O_3 (Indian Rare Earth Ltd., India, purity 99.5 %). Stoichiometric amounts of compounds were mixed in an agate mortar pestle for 3 h using acetone as the mixing medium. The mixed powders were dried by keeping them in an oven overnight. The dried powders were calcined twice at 1000 °C for 6 h in an alumina crucible. The calcined powders were further ground to fine powders and pelletized at an optimum load of 3 tons. These pellets were sintered at 1300 °C for 6 h. After sintering, the pellets were cooled to 500 °C at a cooling rate of 5 °C/min in a programmable furnace.

Characterization

A preliminary study on compound formation and structural parameter was carried out using the X-ray diffraction (XRD) technique with an X-ray powder diffractometer (RigakuMiniflex II). The XRD pattern of the calcined powder was recorded at room temperature with $\text{CuK}\alpha_1$ radiation ($\lambda=$

1.5418 Å) in a wide range of Bragg's angles 2θ ($20^\circ \leq 2\theta \leq 80^\circ$) at a scan speed of $4^\circ/\text{min}$. For scanning electron micrographs (SEM) and energy-dispersive X-ray analysis (EDXA), freshly fractured surfaces of the sintered pellets were gold sputtered and scanned in different regions using a JEOL JSM-5800 scanning electron microscope. Raman spectra were recorded using a HORIBA JOBIN YVON LabRAMHR high-resolution Raman microscope. Fourier transform infrared (FTIR) spectra of the sample were recorded using Shimadzu (Model DF 803). The Fourier transform infrared spectrometer was in the wave number range $400\text{--}4000\text{ cm}^{-1}$. Thermal analysis (DTA and TGA curves) of the sample was made using a Perkin-Elmer (Model Pyrix EXST AR 6000) TG-DTA instrument in the temperature range $30\text{--}950\text{ }^\circ\text{C}$ with a heating rate of $10\text{ }^\circ\text{C}/\text{min}$ in a nitrogen atmosphere.

For impedance measurements, polished surfaces of the pellets were coated with high-purity air-drying silver paste. These pellets were cured at $700\text{ }^\circ\text{C}$ for 10 min. Impedance measurements were done using a computer-controlled impedance analyzer (HP 4192 A LF) over a wide range of temperatures ($50\text{--}650\text{ }^\circ\text{C}$) and frequencies ($10\text{ Hz--}13\text{ MHz}$).

Results and discussion

Crystal structural analysis

X-ray diffraction (XRD) patterns of samples BS, BSL1, BSL5, and BSL10 are shown in Fig. 1. The XRD pattern of samples BS, BSL1, and BSL5 revealed the formation of a

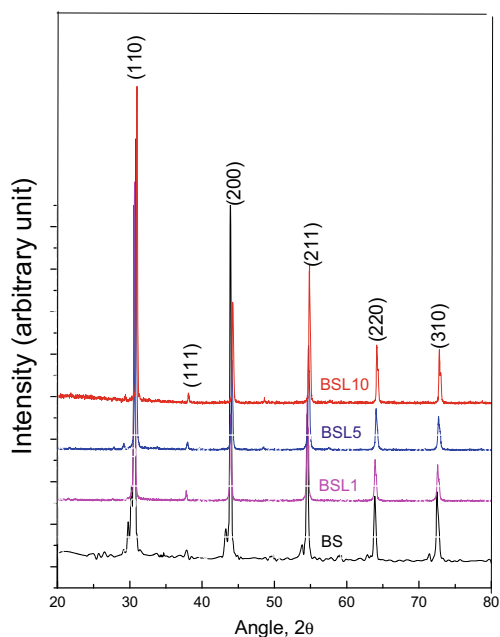


Fig. 1 XRD pattern of the samples in the system $\text{Ba}_{1-x}\text{La}_x\text{SnO}_3$

single-phase solid solution. Formation of the single phase was confirmed on the basis of the absence of characteristic lines of the constituent oxides or other phases in the powder XRD patterns. The XRD pattern of sample BSL10 revealed an extra peak (around an angle of 29°) of reflections from the plane of pyrochlore phase $\text{La}_2\text{Sn}_2\text{O}_7$. It is observed that the intensity of this reflection is weak as compared to the intensity of reflections from the planes of $\text{Ba}_{1-x}\text{La}_x\text{SnO}_3$. A weak intensity of reflections from the planes of pyrochlore phase $\text{La}_2\text{Sn}_2\text{O}_7$ suggests that the volume fraction of the secondary phase is very small as compared to primary phase $\text{Ba}_{1-x}\text{La}_x\text{SnO}_3$. Therefore, the XRD data of all the compositions is indexed on the basis of the cubic unit cell similar to undoped BaSnO_3 reported in the literature (JCPDS card no. 15-0780). The lattice parameter of the samples was calculated using the program CELL. The value of the lattice parameter for all the compositions is given in Table 1. From the table, one infers that the lattice parameter decreases with increasing x , i.e., lanthanum concentration. The decrease in the lattice parameter from samples BS to BSL10 is attributed to smaller ionic radii of La^{3+} (1.32 \AA) as compared to host Ba^{2+} (1.44 \AA) ion.

The crystallite size of the synthesized compositions was calculated using the Debye–Scherrer equation $D=0.9\lambda/\beta\cos\theta_{\text{max}}$ (where D is the crystallite size, λ is the wavelength of $\text{CuK}\alpha$ radiation, β is the line width at half peak intensity, and θ_{max} is the diffraction peak angle). The average crystallite size determined from the most intense peak of plane (110) for all the samples is given in Table 1.

The bulk density (d_b) of the samples was obtained using Archimedes' principle. The theoretical density (d_{th}) of the samples was calculated from the molecular weight of the samples and its lattice parameter. The percentage porosity was calculated using the formula:

$$\% \text{ porosity} = [(d_{\text{th}} - d_b)/(d_{\text{th}})] \times 100 \quad (1)$$

The bulk density, theoretical density, and percentage porosity of the samples is given in Table 1.

SEM and EDXA analyses

The SEM surface morphology of the samples is shown in Fig. 2. It is observed that the grain size of the samples is small ($<1\text{ }\mu\text{m}$). The porous nature of the samples is also reflected in the SEM photographs. The compositional homogeneity (in terms of the concentration profile of the elements) has been probed by recording the EDXA spectrum of randomly chosen different regions on the surfaces of the samples. Figure 3 depicts the EDXA spectra (corresponding to that region whose microstructure are given in Fig. 2) of the samples. It shows that in these samples, only oxygen, tin, barium, and lanthanum elements are present. The positions of all the peaks observed

Table 1 Crystallite size, lattice parameter, theoretical density, experimental density, percentage porosity, and conductivity of the samples in the system $\text{Ba}_{1-x}\text{La}_x\text{SnO}_3$

S. no.	Sample	Crystallite size of sintered powder (nm)	Lattice parameter (Å)	Theoretical density (g/cc)	Experimental density (g/cc)	Percentage porosity	Total conductivity, σ_t ($\Omega \text{ cm}$) ⁻¹ at 30 °C
1.	BS	56	4.1181±0.0002	7.22	6.82	14	1.37×10 ⁻⁷
2.	BSL1	53	4.1168±0.0004	7.24	5.81	20	4.03×10 ⁻⁷
3.	BSL5	58	4.1074±0.0003	7.29	5.62	23	9.46×10 ⁻⁴
4.	BSL10	64	4.0987±0.0002	7.39	5.37	27	1.52×10 ⁻³

in Fig. 3a are in agreement with the EDXA pattern reported for BaSnO_3 [32]. In the literature, it is reported that the positions of the Ba and La peaks are the same (i.e., almost at the same energy value); therefore, the peaks of La are masked by the peaks of Ba [33]. The average value (using data recorded for different regions) of the weight percent and atomic percent of different elements for all the samples is reported in Table 2. The atomic ratio of Sn/Ba for all the samples is in agreement with the theoretical ratio which confirms doping of lanthanum on the barium site in BaSnO_3 .

Raman spectroscopy

Raman spectroscopy is yet another tool to explore the incorporation of dopants in the host lattice as it is very sensitive to (local) loss of symmetry and formation of defects such as oxygen vacancies and F-centers [34, 35]. The room temperature Raman spectra ranging from 50 to 800 cm^{-1} of undoped BaSnO_3 (BSL0) and La-doped BaSnO_3 (BSL1 and BSL10) samples is shown in Fig. 4. In principle, the centrosymmetric BaSnO_3 with the ideal cubic structure belonging to the space group $\text{Pm}3\text{m}$ should not show first-order Raman

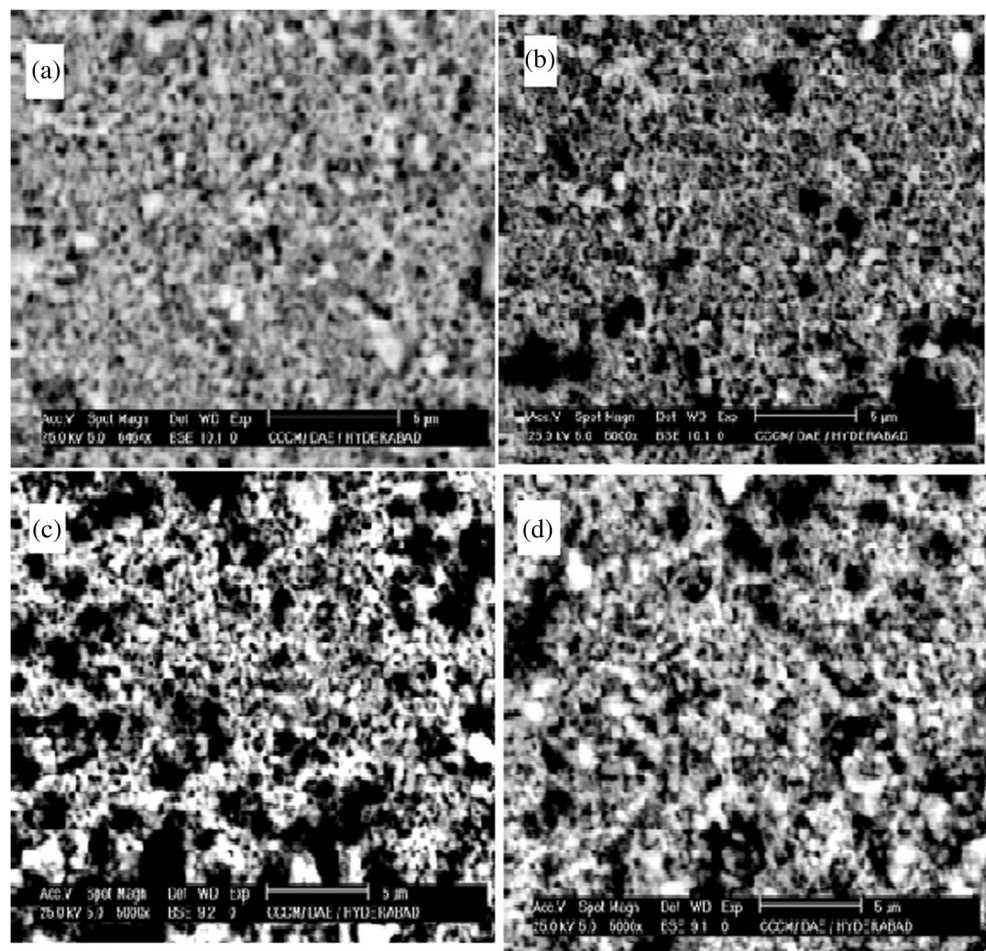
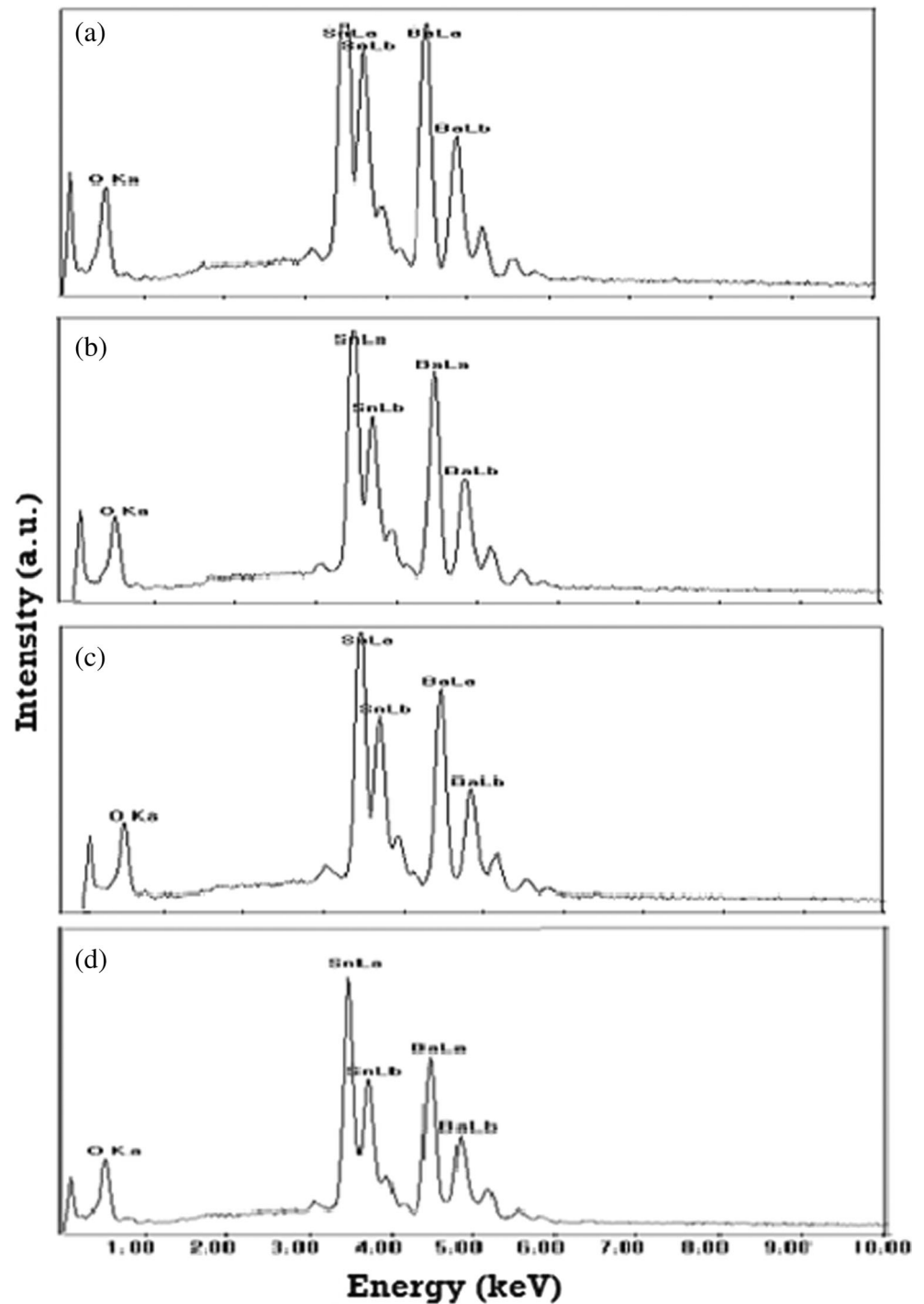
Fig. 2 Scanning electron micrographs of the samples **a** BS, **b** BSL1, **c** BSL5, and **d** BSL10

Fig. 3 Energy-dispersive X-ray (EDX) spectra of the samples **a** BS, **b** BSL1, **c** BSL5, and **d** BSL10



scattering [36]. But Fig. 5 exhibits a batch of Raman active modes for all the samples. The Raman active modes for these samples are in agreement with the Raman spectra reported in the literature for undoped and La-doped BaSnO_3 samples [37, 38]. Raman active modes in undoped BaSnO_3 are induced by defects such as oxygen vacancies which destroy the translational periodicity of the lattice. In the literature, the position of the Raman

line for oxygen vacancies is reported to be at 568 cm^{-1} [39]. This mode is present in all samples, but its intensity increases with an increasing content of La. Two broad modes (at 129 and 225 cm^{-1}) of BaSnO_3 are getting sharpened and shifted towards the lower frequency side on doping La^{3+} at the Ba^{2+} sites. Moreover, in comparison with Raman spectra of BSL0 and BSL1 samples, two weak modes corresponding to pyrochlore phase $\text{La}_2\text{Sn}_2\text{O}_7$ at 301 and 495 cm^{-1} [40] were

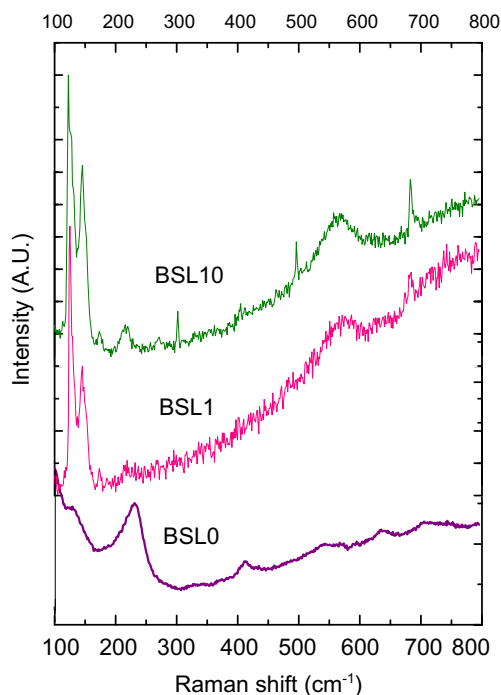
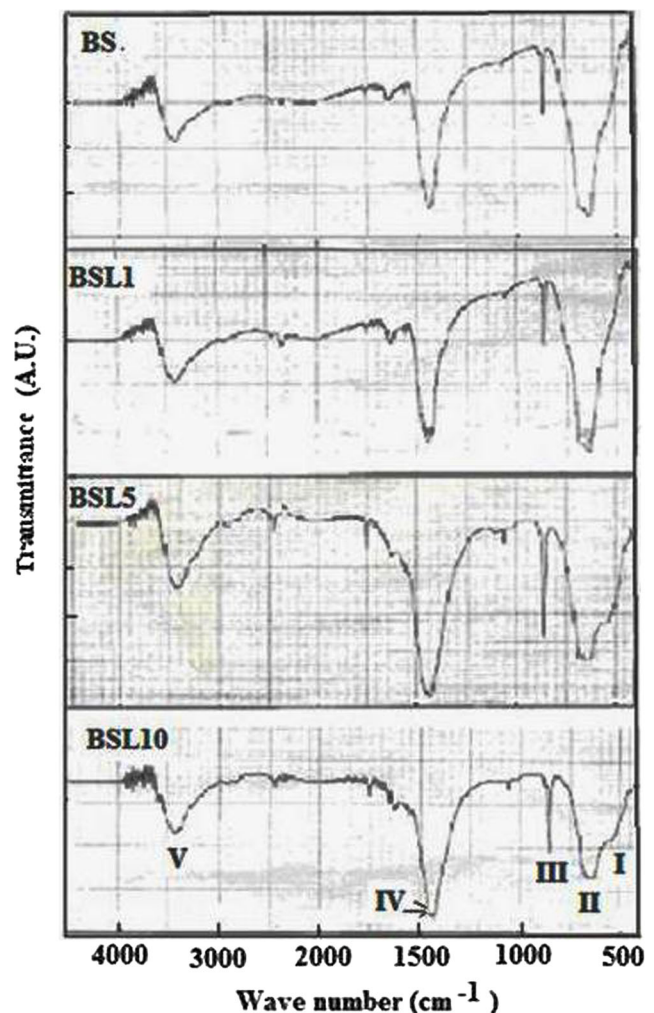
Table 2 Concentration profile of elements by energy-dispersive X-ray analysis (EDXA) of the samples in the system $\text{Ba}_{1-x}\text{La}_x\text{SnO}_3$

Element	BS		BSL1		BSL5		BSL10	
	wt%	at.%	wt%	at.%	wt%	at.%	wt%	at.%
O K	18.64	62.93	18.05	62.94	18.11	62.81	18.11	62.86
Sn L	38.45	18.62	39.01	18.61	38.81	18.40	38.70	18.57
Ba L	42.91	18.45	42.48	18.20	41.13	17.46	39.64	16.65
La L	–	–	00.46	00.25	01.95	01.33	03.55	01.92

detected in the BSL10 sample, demonstrating the presence of the secondary phase, analogous to XRD results.

FTIR spectroscopy

To obtain the Fourier transform infrared (FTIR) spectrum of the samples, small amounts of the powders were mixed with KBr and pelletized again using a hydraulic press. The FTIR spectrum of the KBr mixed pellets was recorded in the wave number range $400\text{--}4000\text{ cm}^{-1}$. The FTIR spectrum of the synthesized samples is shown in Fig. 5. It is noticed that the FTIR spectrum of these samples has mainly five absorption bands. The position of these bands in terms of wave number (cm^{-1}) is presented in Table 3. These bands are marked as I, II, III, IV, and V in Fig. 5. Absorption band I present in samples BSL5 and BSL10 is assigned to vibration from hydroxyl metals (Sn-OH) [41], band II to the Sn-O bond, i.e., structural

**Fig. 4** Room temperature Raman spectra of the samples in the system $\text{Ba}_{1-x}\text{La}_x\text{SnO}_3$ **Fig. 5** FTIR spectra of the samples in the system $\text{Ba}_{1-x}\text{La}_x\text{SnO}_3$

development of perovskite phase [42], and band III to BaCO_3 [43]. An intense band IV can be assigned to either BaCO_3 and/or M-OH group vibration [43, 44]. The broad band V indicates water in the sample which is absorbed from the atmosphere either by the samples and/or by the KBr pellet [45].

From the Table 3, it is noticed that the position of band II shifts systematically towards a higher wave number, i.e., towards higher energy with increasing concentration of dopant

Table 3 Fourier transformation infrared (FTIR) data of the samples in the system $\text{Ba}_{1-x}\text{La}_x\text{SnO}_3$

Samples	Position of the peak (cm^{-1})				
	I	II	III	IV	V
BS	–	626	858	1419	3450
BSL1	–	638	856	1441	3450
BSL5	544	648	856	1444	3450
BSL10	550	652	858	1454	3450

La. Since ionic radii of the barium ion are larger than those of the lanthanum ion ($R_{La^{3+}} < R_{Ba^{2+}}$), when La is incorporated at the Ba site, the lattice parameter and unit size decrease. The decrease in the lattice parameter with the increasing concentration of La was experimentally observed from the X-ray studies of the samples (Fig. 1). A decrease in the unit cell size shortens the distance between Sn^{4+} ion and O^{2-} ion, enhancing the bond strength. Similar results have been reported for the La-doped $BaTiO_3$ samples [46].

It is mentioned in the literature that absorption bands at 856, 1050, and 1450 cm^{-1} are the characteristic bands of $BaCO_3$ [43]. The presence of bands III and IV indicate that sintered powders have $BaCO_3$ as the impurity phase. This result is in contradiction to the result obtained from the X-ray diffraction analysis. From the JCPDS (file no. 45-1471) file of $BaCO_3$, it has been found that $BaCO_3$ has a strong peak at 23.98°. In the XRD pattern of the samples (Fig. 1), no peak at this angle has been observed. Absence of the peak of $BaCO_3$ in the XRD pattern of the samples may be due to the fact that any $BaCO_3$ left was amorphous, or present as very small crystallites which were below the critical size for Bragg reflection. But strong intensity and XRD results indicate that this band is not merely due to the presence of a trace amount of $BaCO_3$. It is already mentioned that peak IV may be due to the presence of the M–OH group. Therefore, it seems that the band due to the presence of $BaCO_3$ and the M–OH group has been integrated in the broad and intense band.

Thermal analysis

The thermal characterization of the synthesized powders has been carried out using differential thermal analysis (DTA) and thermogravimetric analysis (TGA) up to 1000 °C at a heating rate of 10 °C/min in a nitrogen atmosphere. The DTA and TGA curves of samples BSL0, BSL5, and BSL10 are shown in Fig. 6. Similar behavior is observed for sample BSL1 also. The TGA curves of the samples exhibit an approximately 10 % total weight loss in three steps, the first step from RT to 300 °C (with a loss of 4.5 %), the second step from 300 to 550 °C (with a loss of 1 %), and the third step from 550 to 950 °C (with a loss of 4.5 %). The weight loss in the first step is attributed to the removal of physically adsorbed water; that of the second step to the removal of other gases, for example CO_2 ; and that of the third step to the removal of chemically adsorbed water. The presence of water or the hygroscopic nature of these samples is also reflected from FTIR spectra of the samples.

The enthalpy changes observed in the DTA curve at different temperatures can be attributed to surface reaction taking place in the BS sample. There is no evidence of any phase transition taking place in the samples up to 1000 °C.

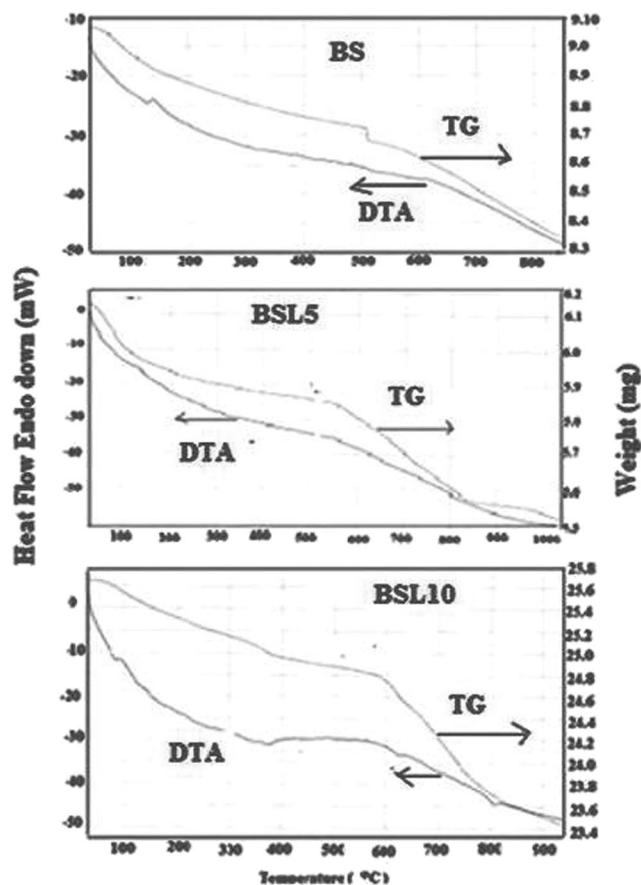


Fig. 6 Thermal analysis (TG-DTA) curve of the samples in the system $Ba_{1-x}La_xSnO_3$

Impedance analysis

From Table 2, it is noticed that the conductivity of the samples increases sharply when x changes from 0 to 0.10. For the sake of clarity, the variation of total conductivity σ_t (at room temperature) with a concentration of lanthanum is shown in Fig. 7. The observed sharp increase in the conductivity

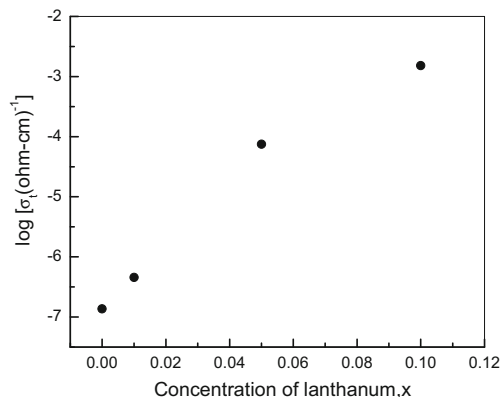
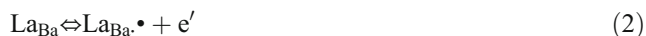


Fig. 7 Variation of the logarithm of conductivity with the concentration of the dopant in the system $Ba_{1-x}La_xSnO_3$

(approximately by four orders of magnitude) on doping La^{3+} at the Ba^{2+} (up to 10 mol%) site in barium stannate is believed to be due to the dissolution of La^{3+} (hetero-cation) at Ba^{2+} sites within the perovskite structure. An increase in conductivity with increasing lanthanum concentration indicates that electronic charge compensation is taking place according to the equation:



All the samples in the present system, $\text{Ba}_{1-x}\text{La}_x\text{SnO}_3$, have been synthesized by the solid state ceramic route at a temperature of 1300 °C; therefore, the loss of oxygen takes place according to the equation



The sharp increase of conductivity from samples BSL0 to BSL10 reveals that global electrons are arising from both Eqs. (2) and (3). The increasing lanthanum concentration at the barium site of barium stannate increases its electronic conductivity.

Complex impedance data of samples BSL5 and BSL10 could not be recorded on account of the high value of conductivity. Complex impedance data of sample BS are already published [47]; therefore, complex plane impedance data of sample BSL1 are presented. Impedance plots of sample BSL1 at different temperatures are shown in Fig. 8. At temperatures 50, 100, and 150 °C, a steep rising of Z'' (almost parallel to the Y -axis) is observed. As the temperature increases to 200 and 250 °C, the curve bends towards the real axis, i.e., Z' axis, and takes the shape of a semicircle. At and above 300 °C, two distinct semicircular arcs have been observed. The frequency ranges of these arcs overlap. The high-frequency arc at 300 and 350 °C passes through the origin, but the spectrum at 400 °C and above does not pass through the origin. An intercept of approximately 450 Ω is observed which remains almost constant up to the last temperature of measurement, i.e., up to 650 °C. At all the temperatures, the centers of the semicircles are below the real axis, i.e., depressed semicircles have been observed.

For samples in the present system, $\text{Ba}_{1-x}\text{La}_x\text{SnO}_3$, the electrode contribution to the impedance data is ruled out on account of the linear V - I characteristics of the samples at room temperature. Therefore, the total impedance has contributions of the grains and grain boundaries. In impedance plots of sample BSL1, two arcs have been observed, and their characteristic frequency, $\omega_o = 1/\rho\epsilon_o\epsilon$, differs significantly. The question of whether $\omega_{o,g}$ and $\omega_{o,gb}$ are significantly different

from one another reduces to the question of whether or not the products $(\rho_g\epsilon_g)$ and $(\rho_{gb}\epsilon_{gb})$ differ significantly. While the resistances of the materials cover many orders of magnitude, the dielectric constant does not vary that significantly. Thus, it is reasonable to make the assumption that $\epsilon_g \approx \epsilon_{gb}$ and the question reduces further to whether or not ρ_g and ρ_{gb} are significantly different from one another. For a material in which $\sigma_g > \sigma_{gb}$ (by definition $\rho_{gb} > \rho_g$), it is implied that $\omega_{o,gb} < \omega_{o,g}$. Consequently, two arcs will be present in the complex plane impedance plot, and the arc at the lower frequency will indeed correspond to the response of the grain boundaries whereas the high-frequency arc will correspond to the response of the grains. The resistance of each arc is given by the distance across the real axis that each arc spans. In addition, the equivalent capacitance, C , of each arc is given by $(R\omega_o)^{-1}$. It is reported that in the impedance plot of a polycrystalline material, two arcs only appear when condition $\sigma_g > \sigma_{gb}$ is satisfied, if a material has the typical microstructure, i.e., $g/G < 1$ (where G is the average diameter of the grains and g is the grain boundary thickness).

Impedance spectra of the sample BSL1 were fitted using the equivalent circuit containing two parallel resistance(R)–capacitance (C) connected in series, one for the bulk and other for the grain boundaries. The values of resistances and capacitances at different temperatures are obtained from the fitting of the data. As an example, best fitting of impedance spectra yielded parameters $R_g = 161,000 \Omega$, $C_g = 1.56 \times 10^{-11} \text{ F}$, $R_{gb} = 163,000 \Omega$, and $C_{gb} = 48.8 \times 10^{-11} \text{ F}$ at 300°. Total resistance of the sample is given by $R_t = R_g + R_{gb}$. Total conductivity (σ_t) has been determined using the formula

$$\sigma_t = [(1)/(R_g + R_{gb})] \times (L/S) \quad (3)$$

where L is the thickness and S is the area of the sample. Similarly, the grain conductivity (σ_g) and apparent grain boundary conductivity (σ_{gb}) can be determined separately.

According to Verkerk [48] and Christie et al. [49], there exists a relation between the apparent grain boundary conductivity (σ_{gb}) determined from the grain boundary arc of the impedance plot and the specific grain boundary conductivity σ_{gb}^* as given by Eq. (4):

$$\sigma_{gb}^* = (\delta_{gb}/d_g)\sigma_{gb} \quad (4)$$

where δ_{gb} is the thickness of the grain boundary and d_g is the average grain size. If bulk and grain boundary

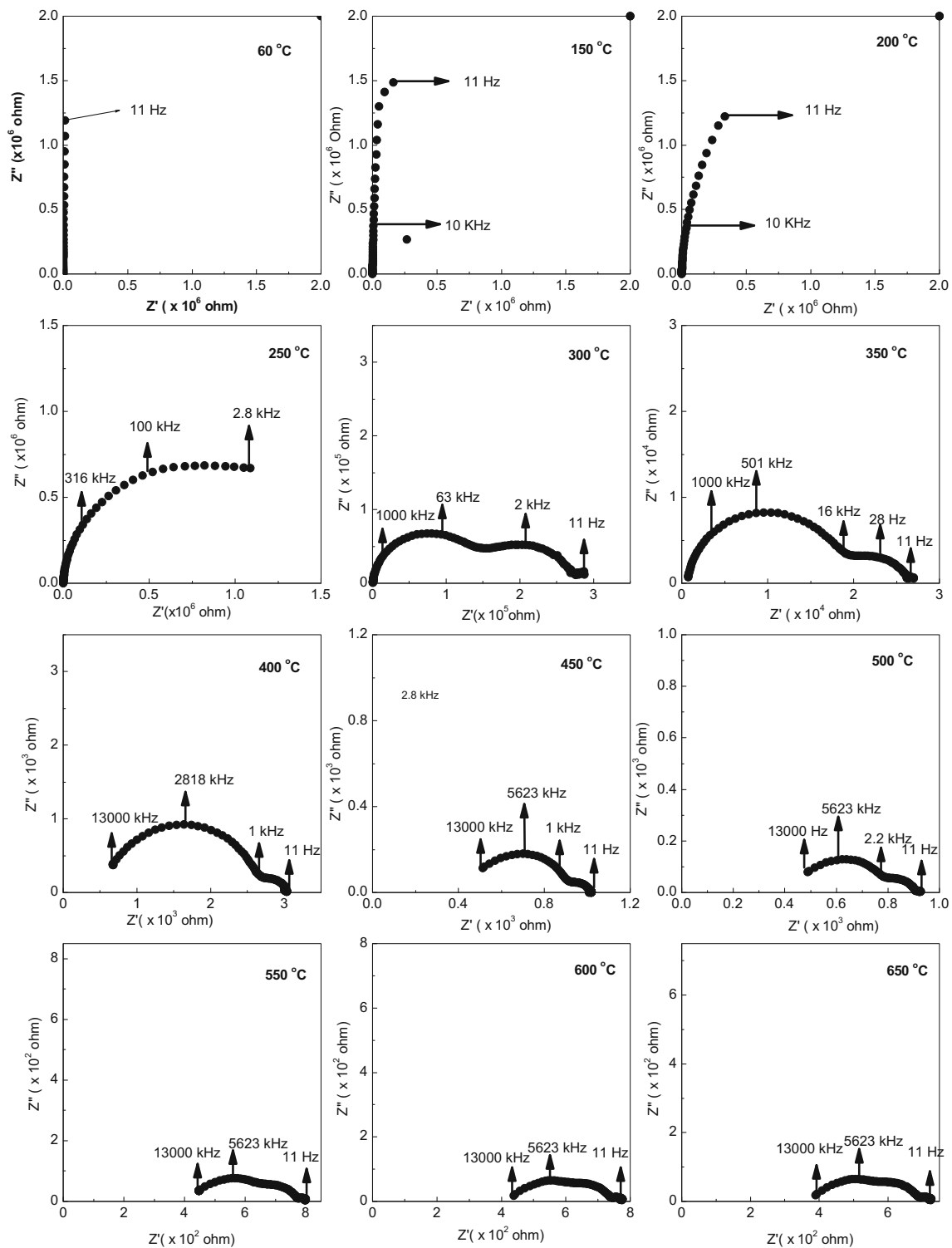


Fig. 8 Complex plane impedance plots of the sample BSL1 at different temperatures

permittivities are similar, then Eq. (5) can be written as

$$\sigma_{gb}^* = (C_g/C_{gb})\sigma_{gb} \tag{5}$$

where C_g and C_{gb} are the bulk and grain boundary capacitances determined from the impedance plots.

The variation of logarithm of the total conductivity (σ_t), grain conductivity (σ_g), and specific grain boundary conductivity (σ_{gb}^*) with the inverse of temperature is

shown in Fig. 9. Two linear regions with different slopes in two different temperature regions have been observed. These two temperature regions are denoted as region I (300–450 °C) and region II (450–650 °C). The linear behavior of conductivities in both the temperature regions indicates that these resistances obey the Arrhenius relation given by

$$\begin{aligned}\sigma_t &= \sigma_{ot}(1/T)\exp(-E_t/kT) \\ \sigma_g &= \sigma_{og}(1/T)\exp(-E_g/kT) \\ \sigma_{gb}^* &= \sigma_{ogb}^*(1/T)\exp(-E_{gb}/kT)\end{aligned}\quad (6)$$

where σ_{ot} is the pre-exponential factor, k is the Boltzmann constant, and T is the absolute temperature. Values of

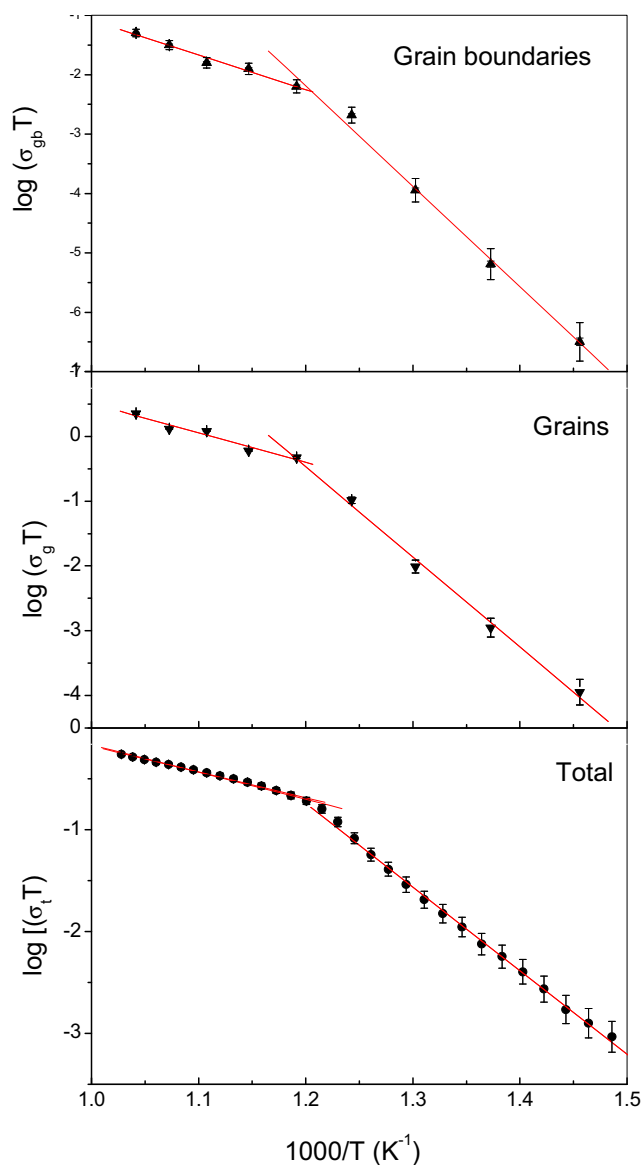
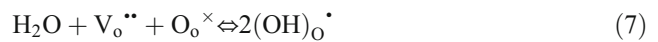


Fig. 9 Variation of logarithm of total, grain, and grain boundary conductivities with inverse of temperature for sample BSL1

activation energy of the bulk ionic conductivity (E_t) for the sample determined from the plot by least square fitting of the data points in Fig. 9 are given in Table 4. The value of activation energy in the low-temperature region varies from 1.14 to 1.39 eV and in the high-temperature region from 0.37 to 0.51 eV.

Samples in the present study have been synthesized by the solid state ceramic route at 1300 °C; therefore, there is a possibility that oxygen leaves the lattice according to Eq. (6). The possibility of oxygen vacancies in the sample cannot be ruled out. It is reported that oxygen vacancies (V_o^{**}) are highly mobile in the perovskite structure and the activation energy for diffusion of these vacancies is approximately 1 eV [50, 51]. Therefore, conduction in the low-temperature range (region I) is proposed to take place due to the motion of doubly ionized oxygen vacancies (V_o^{**}).

In the literature, the activation energy for proton conduction in perovskite materials is reported to be between 0.40 and 0.50 eV [52, 53]. The activation energy in the high-temperature range (region II) of the sample lies between 0.39 and 0.52 eV. It is also reported in the literature that in the FTIR spectrum of high-temperature proton conductors, an intense band at 1420 cm^{-1} appears due to the presence of OH^- groups [44]. In the FTIR spectrum (Fig. 5) of sample BSL1, an intense band around 1420 cm^{-1} is also present. Therefore, the possibility of conduction in the sample BSL1 in the high temperature range (region II) by protonic defects cannot be ruled out. This sample has a porosity of approximately 20 %; hence, if electrical properties are measured in an ambient atmosphere, water molecules can be adsorbed by the materials. Adsorption of water molecules by these materials has been confirmed from their FTIR spectrum (Fig. 5) and thermal analysis (Fig. 6). Incorporation of adsorbed water molecules into the oxide lattice can be represented as the process of dissociative dissolution and formation of protonic defect according to reaction (7):



In the above reaction, oxygen vacancies are consumed to produce twice the protonic defect. It seems that in the present sample, the above reaction is taking place at a higher temperature ($T \geq 450\text{ °C}$). A high concentration of protonic defects

Table 4 Total conductivity at 650 °C (σ_t); activation energy of grains (E_g), grain boundaries (E_{gb}), and total (E_t); and thickness of the grain boundaries (δ_{gb}) of sample BSL1

Temperature range (°C)	E_g (eV)	E_{gb} (eV)	E_t (eV)
250–400	0.42 ± 0.04	0.57 ± 0.02	0.50 ± 0.02
400–650	1.38 ± 0.03	1.69 ± 0.03	1.63 ± 0.02

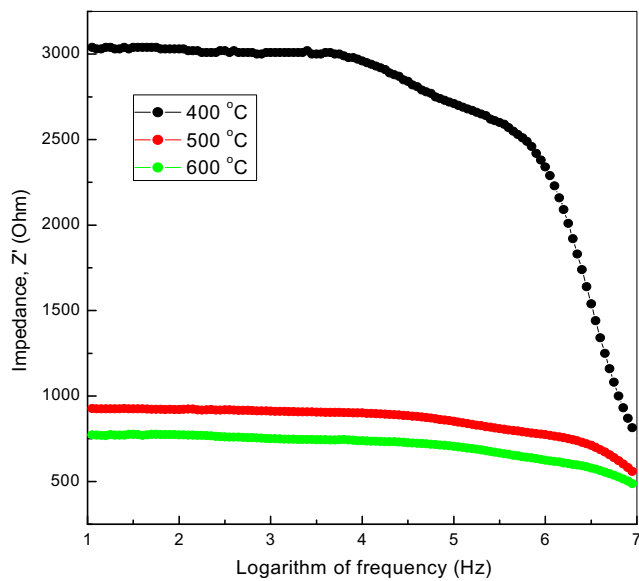


Fig. 10 Variation of the real part of impedance (Z') with the logarithm of frequency at three different temperatures

with respect to that of oxygen ion vacancies may lead to the change in the conduction mechanism with increasing temperature. At and above 450 °C temperature, protonic defects may be the dominant charge carrier and govern the conduction mechanism. These protons (OH^+) may hop from one oxygen vacancy $V_{\text{O}}^{\bullet\bullet}$ to another one. Similar activation energy of both resistances shows that a sufficient amount of protons (OH^+) is present in the bulk (grain) of the material, i.e., adsorption of water molecules is not limited to the surface but it has penetrated through grains. It is worthwhile to mention that in the synthesis of this sample, water has not been used at any stage.

Figure 10 shows the variation of the real part of impedance (Z') as a function of frequency at three different temperatures. A similar behavior is observed at higher temperatures also. The presence of two relaxation processes is clearly seen in these plots. It is also clear that the relaxation time of these processes is temperature dependent. The trend of impedance vs. frequency plot provides an indication of increasing conduction with frequency and temperature (i.e.,

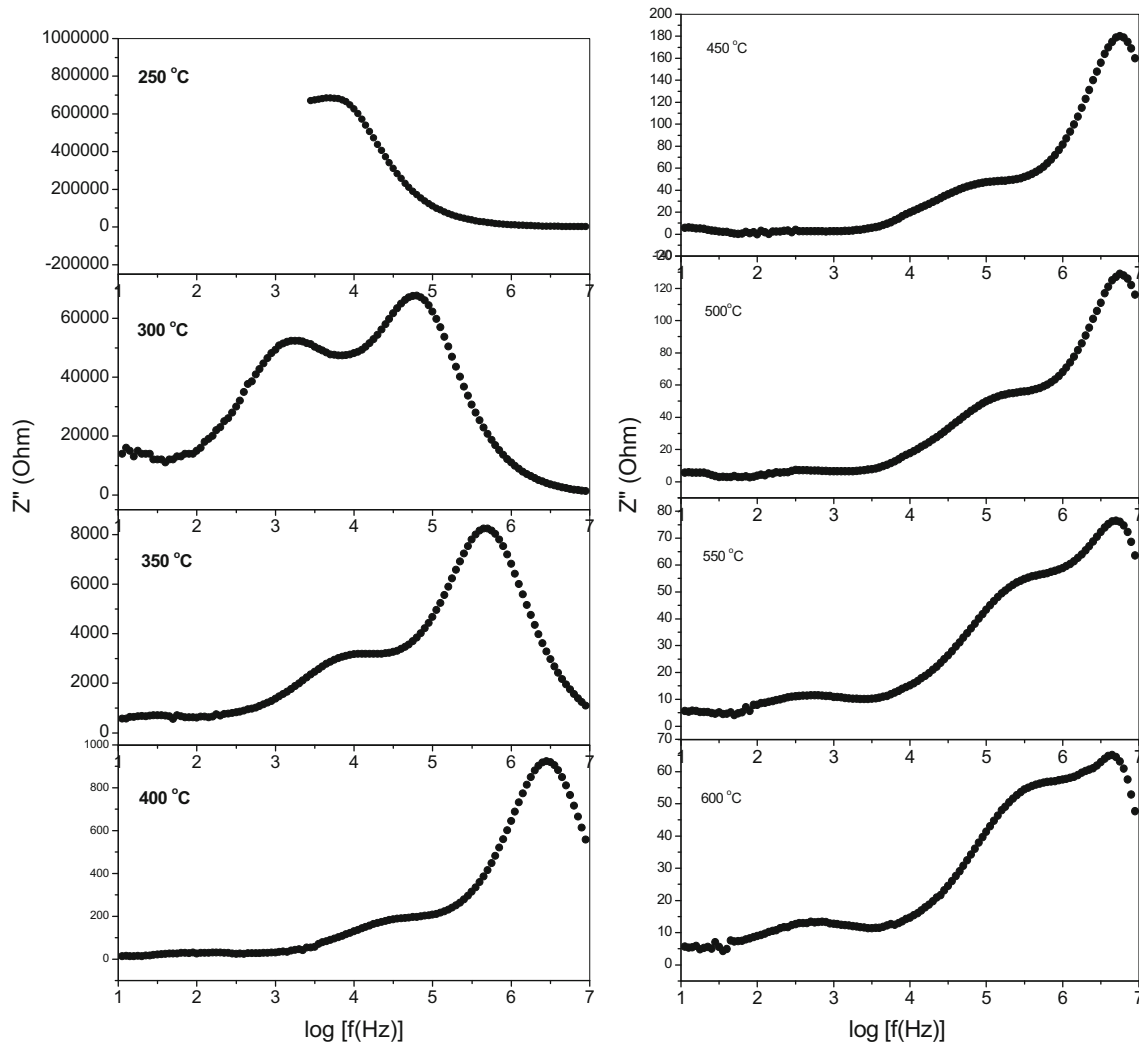


Fig. 11 Variation of the imaginary part of impedance (Z'') with the logarithm of frequency at a few temperatures

negative temperature coefficient (NTC) of resistance behavior typical of semiconductors). Total impedance at 10 Hz frequency (since 10 Hz frequency data is very much close to the d.c. value) at different temperatures is obtained from Fig. 10. Using these data, the total d.c. conductivity of the sample is calculated at different temperatures, to attain a maximum value of $5.35 \times 10^{-4} (\Omega \text{ cm})^{-1}$ at 650 °C. On comparing the conductivity value of this sample with the conductivity value of acceptor (La, Y, In, Gd, etc.)-doped barium stannate systems reported to be high-temperature proton conductors [22], it is found that the conductivity of sample BSL1 is almost equal to the conductivity of the above-mentioned acceptor-doped barium stannate systems.

The variation of Z'' with the logarithm of frequency at different temperatures is shown in Fig. 11. It is observed that at and above 300 °C, two peaks are present in these plots. The position of each peak shifts towards the higher frequency side with increasing temperature. The heights of these peaks decrease with an increase in temperature. A typical peak broadening which is slightly asymmetrical in nature can also be observed with a rise in temperature. Broadening in the low-frequency peak is more than broadening in the high-frequency peak. Moreover, broadening in peak is independent of temperature. This suggests that there is a spread of relaxation time, i.e., the temperature-dependent electrical relaxation phenomenon exists in the material. However, for the present sample, FWHM is >1.144 decades for both the peaks, which is attributed to the distribution of relaxation time. A peak is observed when the relation $\omega\tau=1$ is satisfied (ω —angular frequency is equal to $2\pi f$, f being the frequency (Hz) and τ , the relaxation time). With an increase in temperature, the relation $\omega\tau=1$ is satisfied at a higher frequency. The relaxation time τ for grains and grain boundaries is determined from the peak position, and plots of $\log \tau$ (relaxation time) with the inverse of temperature for all the three contributions are shown in Fig. 12. Variation of $\log \tau_g$ with the inverse of temperature shows a single linear region in the entire range of temperatures. The linear behavior of $\log \tau_g$ with $1000/T$ indicates that the relaxation time obeys the Arrhenius relation given by

$$\tau_g = \tau_{g0} \exp(E_\tau/k_B T) \quad (8)$$

where τ_{g0} is the relaxation time at infinite temperature, E_τ the activation energy for relaxation, k_B Boltzmann's constant, and T the absolute temperature. A linear fit of $\log \tau$ vs. $1000/T$ plots has been used to estimate the activation energy of the material. The values so obtained are recorded in Table 4. This value of activation energy (E_τ) estimated for grains at low temperature (≤ 450 °C) when compared with the activation energy value (E_a) is observed to have approximately the same value, well within the experimental error. This result possibly provides an indication that electrical species (charge carriers)

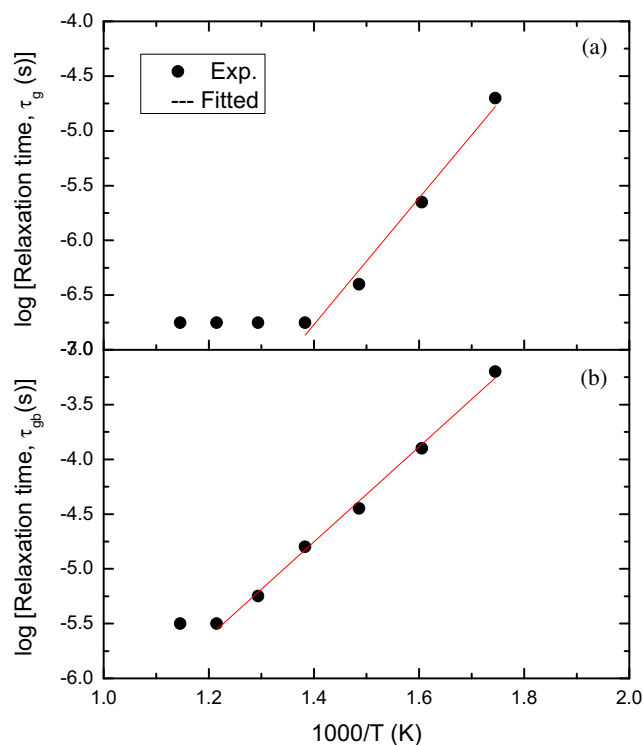


Fig. 12 Variation of the logarithm of relaxation time, τ (obtained from Fig. 10) of **a** grains and **b** grain boundaries

involved in the process of relaxation and conduction for the grains in the low-temperature range are the same. This result possibly provides an indication that electrical species (charge carriers) involved in the process of relaxation and conduction are different.

Conclusions

Powder X-ray diffraction studies confirm the formation of a single phase only up to $0.05 \leq x$. All the samples have a cubic crystal structure. Scanning electron microscopy has confirmed the polycrystalline texture of the material with porous microstructure. EDX analysis confirmed the homogeneous nature of the synthesized material. The FTIR spectrum and TGA curve of the samples exhibited the adsorption of water molecules by the synthesized powders. AC impedance analysis reveals that the total impedance is the contribution of grains and grain boundaries. Two temperature ranges with different activation energies have been observed for both the resistances. The activation energies in both the temperature ranges for both the resistances match well. Therefore, it is concluded that conduction species (phases) responsible for conduction within grains and grain boundaries electrode are the same. The activation energy estimated from the variation of resistances/total resistivity confirmed that conduction in the low-temperature region (300–450 °C) is due to thermal diffusion of doubly

ionized oxygen vacancies ($V_{O}^{\bullet\bullet}$) whereas in the high-temperature region (450–650 °C), it is due to hopping of $(OH)^{\bullet}$ ions. Based on the high-temperature conduction mechanism and similar activation energy for both grains and grain boundaries, it is concluded that even the donor doped barium stannate for high-temperature proton conductors.

Acknowledgments The authors are grateful to the heads of the Department of Physics, Department of Ceramic Engineering, and Department of Chemical Engineering, IIT (BHU), for providing facilities required for the characterization of the samples. The authors are also grateful to Dr. R.K. Singh, Professor, Department of Physics, Science Faculty, BHU, Varanasi, for providing facilities to record the Raman spectra of the samples.

References

- Vivekanandan R, Kutty TRN (1990) Grain boundary layer ceramic capacitors based on donor-doped $Ba(Ti_{1-x}Sn_x)O$. *Mater Sci Eng B* 6:221–231
- Zhou ZG, Zhao G, Wei M, Zhang ZT (1989) Temperature–humidity–gas multifunctional sensitive ceramics. *Sensors Actuators* 19: 71–81
- Singh P, Brandenburg BJ, Sebastian CP, Singh P, Singh S, Kumar D, Parkash O (2008) Electronic structure, electrical and dielectric properties of $BaSnO_3$ below 300 K. *Jpn J Appl Phys* 47:3540–3545
- Movchikova A, Malyshekina O, Suchanek G, Gerlach G, Steinhäuser R, Langhammer HT, Pientischke C, Beige H (2008) Study of the pyroelectric behavior of $BaTi_{1-x}Sn_xO_3$ piezo-ceramics. *J Electroceram* 20:43–46
- Wang T, Chen XM, Zheng XH (2003) Dielectric characteristics and tunability of barium stannatetitanate ceramics. *J Electroceram* 11: 173–178
- Ostrick B, Fleischer M, Lampe U, Meixner H (1997) Preparation of stoichiometric barium stannate thin films: hall measurements and gas sensitivities. *Sensors Actuators B* 44:601–606
- Tao S, Gao F, Liu X, Sørensen OT (2000) Ethanol-sensing characteristics of barium stannate prepared by chemical precipitation. *Sensors Actuators B* 71:223–227
- Lampe U, Gerblinger J, Meixner H (1995) Carbon-monoxide sensors based on thin films of $BaSnO_3$. *Sensors Actuators B* 24–25: 657–660
- Hodjati S, Vaezzadeh K, Petit C, Pitchon V, Kiennemann A (2000) NO_x absorption–desorption study: application to diesel and lean-burn exhaust gas (selective NO_x recirculation technique). *Catal Today* 59:323–334
- McGeehin P and Williams DE (1993) Sensing gaseous substances international application, Patent No WO 9308467 A1 19930429. Indian Institute of Technology (Banaras Hindu University), Varanasi
- Gopal Reddy CV, Manorama SV, Rao VJ (2001) Preparation and characterization of barium stannate: application as a liquefied petroleum gas sensor. *J Mater Sci Mater Electron* 12:137–142
- Dilute XC (2004) Dilute CH_3SH -sensing characteristics of $BaSnO_3$ thick film sensor. *Mater Sci Eng B* 106:305–307
- Borse PH, Lee JS, Kim HG (2006) Theoretical band energetics of $Ba(M_{0.5}Sn_{0.5})O_3$ for solar photoactive applications. *J Appl Phys* 100:124915–124921
- Borse PH, Joshi UA, Ji SM, Jang JS, Lee JS, Jeong ED, Kim HG (2007) Band gap tuning of lead-substituted $BaSnO_3$ for visible light photocatalysis. *Appl Phys Lett* 90:034103–034111
- Yuan Y, Lv J, Jiang X, Li Z, Yu T, Zou Z, Ye J (2007) Large impact of strontium substitution on photocatalytic water splitting activity of $BaSnO_3$. *Appl Phys Lett* 91:094107–094111
- Mizoguchi H, Woodward PM, Park C, Keszler DA (2004) Strong near-infrared luminescence in $BaSnO_3$. *J Am Chem Soc* 126:9796–9800
- Wang Y, Chesnaud A, Bevilion E, Dezanneau G (2012) Properties of Y-doped $BaSnO_3$ proton conductors. *Solid State Ionics* 214:45–55
- Schober T (1998) Protonic conduction in $Ba_{1-x}Sn_{0.5}O_{2.7}$. *Solid State Ionics* 109:1–11
- Wang Y, Chesnaud A, Bevilion E, Yang J, Dezanneau G (2011) Synthesis, structure and protonic conduction of $BaSn_{0.875}M_{0.125}O_{3-\delta}$ ($M=Sc, Y, In$ and Gd). *Int J Hydrog Energy* 36:7688–7695
- Wang Y, Chesnaud A, Bevilion E, Yang J, Dezanneau G (2011) Influence of ZnO additive on the properties of Y-doped $BaSnO_3$ proton conductor. *Mater Sci Eng B* 176:1178–1183
- Li L, Nino JC (2013) Proton-conducting barium stannates: doping strategies and transport properties. *Int J Hydrog Energy* 38: 1598–1605
- Wang Y (2011) Ph.D. thesis Ecole Centrale Paris. Synthesis and characterization of acceptor-doped barium stannate compounds as proton conductors. Indian Institute of Technology (Banaras Hindu University), Varanasi
- Wang Y, Chesnaud A, Bévilion E, Xiong J, Yang J (2013) Effects of Sn substitution on structural and electrical properties of $BaSn_{0.75}M_{0.25}O_{3-\delta}$ ($M=Sc, In, Y, Gd, Nd$). *J Alloys Compd* 555: 395–401
- Bévilion E, Geneste G, Chesnaud A, Dezanneau G (2008) Ab initio study of La-doped $BaSnO_3$ proton conductor. *Ionics* 14:293–301
- Hadjarab B, Bouguelia A, Trari M (2007) Optical and transport properties of lanthanum-doped stannate $BaSnO_3$. *J Phys D Appl Phys* 40:5833–5839
- Hadjarab B, Bouguelia A, Benchettara A, Trari MA (2008) The transport and photo electrochemical properties of La-doped stannate $BaSnO_3$. *J Alloys Compd* 461:360–366
- Wang HF, Liu Q, Chen ZF, Gao GY, Wu W (2007) Transparent and conductive oxide films with the perovskite structure: La- and Sb-doped $BaSnO_3$. *J Appl Phys* 101:106105-1-3
- Trari M, Doumerc JP, Dordor P, Pouchard M, Behr G, Krabbes G (1994) Preparation and characterization of lanthanum doped $BaSnO_3$. *J Phys Chem Solids* 55:1239–1243
- Yasukawa M, Kono T, Ueda K, Yanagi H, Hosono H (2010) High-temperature thermoelectric properties of La-doped $BaSnO_3$ ceramics. *Mater Sci Eng B* 173:29–32
- Yasuhwa M, Kone T, Ueda K, Yanag H, Kim SW, Hosono H (2013) Thermoelectric properties and figure of merit of perovskite type $Ba_{1-x}La_xSnO_2$ with $x=0.002-0.008$. *Solid State Commun* 173: 49–53
- Upadhyay S, Parkashand O, Kumar D (2004) Synthesis, structure and electrical behaviour of lanthanum-doped barium stannate. *J Phys D Appl Phys* 37:1483–1491
- Azad AM, Hon NC (1998) Characterization of $BaSnO$ -based ceramics part-1: synthesis, processing and microstructural development. *J Alloys Compd* 270:95–106
- Srivastava OP, Kumar N, Sharma IB (2004) Solid state synthesis and structural refinement of polycrystalline $La_xCa_{1-x}TiO_3$ ceramic powder. *Bull Mater Sci* 27:121–126
- Duan LB, Rao GH, Wang YC, Yu J, Wang T (2008) Magnetization and Raman scattering studies of (Co,Mn) codoped ZnO nanoparticles. *J Appl Phys* 104:013909-1–013909-5
- Worlock JM, Porto SPC (1965) Raman scattering by F centre. *Phys Rev Lett* 15:697–99
- Stanislavchuk TN, Sirenko AA, Litvinchuk AP, Luo X, Cheong SW (2012) Electronic band structure and optical phonons of

- BaSnO₃ and Ba_{0.97}La_{0.03}SnO₃ single crystals: theory and experiment. *J Appl Phys* 112:044108
37. Balamurugan K, Harish Kumar N, Balachandran B, Ramachandra Rao MS, Chelvane JA, Santhosh PN (2009) Magnetic and optical properties of Mn-doped BaSnO₃. *Solid State Commun* 49:884–887
 38. James KK, Krishnaprasad PS, Hasna K, Jayaraj MK (2015) Structural and optical properties of La-doped BaSnO₃ thin films grown by PLD. *J Phys Chem Solids* 76:64–69
 39. Gao QQ, Yu QX, Yuan K, Fu XN, Chen B, Zhu CX, Zhu H (2013) Influence of annealing atmosphere on room temperature ferromagnetism of Mn-doped ZnO nanoparticles. *Appl Surf Sci* 264:7–10
 40. Gupta HC, Brown S, Rani N, Gohel VB (2001) A lattice dynamical investigation of the Raman and the infra red frequencies of the cubic A₂Sn₂O₇ pyrochlores. *Int J Inorg Mater* 3:983–986
 41. Ribeiro SJL, Santilli CV, Pulcinelli SH, Fortes FL, Oliveira L (1994) Spectroscopic characterization of SnO₂ gels. *J Sol-Gel Sci Technol* 2:263–267
 42. Gmelin (1975) *Handbuch der Anorganischen Chemie*, Zinn C3, 8 Auflageth edn. Springer, Berlin/Heidelberg, p 193
 43. Deepa AS, Vidya S, Manu PC, Solomon S, John A, Thomas JK (2011) Structural and optical characterization of BaSnO₃, nano powder synthesized through a novel combustion technique. *J Alloys Compd* 509:1830–1835
 44. Animista I, Dogodaeva E, Tarasova N, Kosareva O, Neiman A (2011) Oxygen-ion and proton transport in Ba₄Na₂W₂O₁₁. *Solid State Ionics* 185:1–5
 45. Lu W, Schmidt H (2008) Lyothermal synthesis of nanocrystalline BaSnO₃ powders. *Ceram Int* 34:645–649
 46. Ganguly M, Rout SK, Sinha TP, Sharma SK, Park HY, Ahn CW, Kim IW (2013) Characterization and rietveld refinement of a-site deficient lanthanum doped barium titanate. *J Alloys Compd* 579:473–484
 47. Upadhyay S (2013) High temperature impedance spectroscopy of barium stannate BaSnO₃. *Bull Mater Sci* 36:1019–1036
 48. Verkerk MJ, Middelhuis BJ, Burggraaf AJ (1982) Effect of grain boundaries on conductivity of high purity ZrO₂, Y₂O₃ ceramics. *Solid State Ionics* 6:159–170
 49. Christie GM, Berkel FPF (1996) Microstructure–ionic conductivity relationship in ceria-gadolinia electrolytes. *Solid State Ionics* 83:17–27
 50. Murugraj P, Kreuer KD, He T, Schober T, Maier J (1997) High proton conductivity in barium yttrium stannate Ba₂YSnO_{5.5}. *Solid State Ionics* 98:1–132
 51. Lu W, Jiang S, Zhou D, Gong S (2000) Structural and electrical properties of Ba(Sn, Sb)O₃ electroceramic. *Sensors Actuators A* 80:35–37
 52. Kreuer KD (1999) Aspect of the formation and mobility of protonic charge carriers and the stability of perovskite oxides. *Solid State Ionics* 125:285–302
 53. Kreuer KD (2003) Protonic conducting oxides. *Annu Rev Mater Res* 33:333–359